

Influence of Curvature on Drag Reduction by Opposition Control in Turbulent Flow Along a Thin Cylinder

S. Hara^a, H. Mamori^{a,*}, T. Miyazaki^a

^a*Department of Mechanical and Intelligent Systems Engineering, The University of Electro-Communications, 1-5-1, Chofugaoka, Chofu, Tokyo 182-8585, Japan*

Abstract

Opposition controlled fully developed turbulent flow along a thin cylinder is analyzed by means of direct numerical simulations. The influence of cylinder curvature on the skin-friction drag reduction effect by the classical opposition control (i.e., the radial velocity control) is investigated. The curvature of the cylinder affects the uncontrolled flow statistics; for instance, skin-friction coefficient increases while Reynolds shear stress (RSS) and turbulent intensity decrease. However, the control effect in the case of a small curvature is similar to that in channel flow. When the curvature is large, the maximum drag reduction rate decreased. However, the optimal location of the detection plane is the same as that in a flat plate. Further, the drag reduction effect is achieved even on a high detection plane where the drag increases in the flat plate. Although a difference in the drag reduction effect can be observed with a change in the curvature, its mechanism considered in this analysis based on the transport of the Reynolds stress is similar to that of the flat plate.

Keywords: turbulent flow along a cylinder, drag reduction, opposition control, direct numerical simulation

2016 MSC: 00-01, 99-00

*Corresponding author
Email address: mamori@uec.ac.jp (H. Mamori)

1. Introduction

Flow control to decrease skin-friction drag in turbulent flows is significant in mitigating environmental impacts. To decrease wall turbulence, many control techniques have been examined numerically and experimentally. In particular, active control is of great interest because it has high performance and robustness. Opposition control is one of the active control methods based on the relationship between wall-friction and streamwise vortices near the wall. The drag reduction effect of the opposition control was identified in both fully developed turbulent channel flow (Choi *et al.* [1]; Hammond *et al.* [2]; Chung *et al.* [3]; Deng *et al.* [4]; Ge *et al.* [5]; Wang *et al.* [6]) and boundary layer flow (Stroh *et al.* [7]; Xia *et al.* [8]) through direct numerical simulation (referred as DNS, hereafter) and large eddy simulation.

Reducing skin-friction drag by opposition control was first proposed by Choi *et al.* [1] in numerically simulated turbulent channel flows. The opposition control is formulized as

$$v_w(x, z, t) = -v(x, y_d^+, z, t), \quad (1)$$

where the subscript of 'w' indicates the wall value, superscript '+' indicates the non-dimensional value normalized by the wall viscous unit of the uncontrolled flow, v is the wall-normal velocity, y_d is the detection plane height, t is the time, and x and z denote the streamwise and spanwise coordinates, respectively. They found that drag decreased 25% at the detection surface near the wall ($y_d^+ = 10$) and increased at plane slightly away from the wall ($y_d^+ = 26$). Hammond *et al.* [2] investigated the optimal location of the detection plane where the drag reduction rate was maximized; this was approximately $y_d^+ = 15$ at $\text{Re}_\tau = 180$. In addition, they reported that the control, based on a detection plane far from the wall ($y_d^+ > 20$), responded strongly to sweep and ejection events and increased the drag.

Chung *et al.* [3] and Deng *et al.* [4] extended Eq. (1) to investigate the amplitude dependence of the opposition control as follows:

$$v_w(x, z, t) = -Av(x, y_d^+, z, t). \quad (2)$$

Here, A is the strength of wall blowing and suction. Chung *et al.* [3] conducted
 25 a study in the range of $0 < A < 1$. They showed that A drastically changed
 the drag reduction rate, indicating that it was a parameter as important as the
 detection plane height. In fact, even along the detection plane height where
 the drag increases when $A = 1$, a drag reduction was achieved by reducing A .
 Furthermore, they found that there was a linear relationship independent of A
 30 between the maximum root mean square (rms) value of wall-normal velocity
 (and vorticity) and the drag reduction rate. Deng *et al.* [4] studied the same
 phenomenon in the range of $1 < A < 8$. They reported that increasing A
 decreased the drag regardless of the detection plane height. The maximum
 drag reduction rate was 33% when $y_d^+ = 15$ and $A = 8$.

35 Ge *et al.* [5] analyzed the energy transport through DNS in a turbulent chan-
 nel flow and proposed a mechanism by which opposition control causes drag re-
 duction. They showed that the pressure strain term in the wall-normal direction
 plays a key role in the dynamic evolution of turbulent flow with opposition con-
 trol. Stroh *et al.* [7] and Xia *et al.* [8] performed DNS in a spatially developed
 40 turbulent boundary layer flow with opposition control. Many previous studies
 on opposition control focused on fully developed turbulent channel flow. How-
 ever, general external flow need to consider spatial development. They showed
 that the drag reduction rate was similar to that of the turbulent channel flow,
 while the net energy saving rate and gain were reduced. They argued that the
 45 reason for the decreased net energy saving rate is that the turbulent boundary
 layer flow has high velocity and pressure fluctuations and require large power
 for control.

The turbulent flow along cylinders are important from viewpoints of en-
 gineering applications such as ship hulls, aircraft fuselage, sonar array, and
 50 monofilament yarn. It is an established fact that due to curvature of the cylin-
 der the skin-friction drag coefficient differs from that of the flat plate and there
 are two parameters to characterize the flow: γ ($= \delta^*/a^*$) and a^+ . Here, the
 superscript '*' indicates the dimensional variable, δ is the boundary layer thick-
 ness, and a is the radius of the cylinder.

55 Neves *et al.* [9, 10] conducted a DNS for a turbulent flow along a cylinder. They compared the experimental results and investigated the effect of curvature on the turbulent structure under the conditions of two cases ($\gamma = 5$, $a^+ = 42$ and $\gamma = 11$, $a^+ = 21$). Their DNS results revealed that when a^+ was small, the inner layer was considerably affected by curvature. In fact, as the curvature
60 increased, the skin-friction coefficient also increased while, on the other hand, the mean velocity gradient decreased in the log-law region. Furthermore, the turbulent intensity and the Reynolds shear stress decreased, indicating the same trend as the previous experimental results. Piquet *et al.* [11] and Afzal *et al.* [12] categorized the effects of curvature on the flow:

- 65 – at $\gamma \lesssim 1$ and $a^+ \gtrsim 250$, influence of curvature is very small;
- at $\gamma \gg 1$ and $a^+ \gtrsim 250$, curvature affects the outer layer;
- at $\gamma \gg 1$ and $a^+ \lesssim 250$, curvature affects both the outer layer and the inner layer.

Monte *et al.* [13] derived the identity of the skin-friction coefficient in turbu-
70 lent flows along a cylinder (i.e., known as FIK identity, Fukagata *et al.* [14]) and investigated the Reynolds number dependence of the mean flow and the turbulent contribution term. Ohta [15] implemented DNS at low Reynolds numbers ($120 < Re_a = a^*u_\infty^*/\nu^* < 300$). At their lowest Reynolds number, $Re_a = 120$, the number of high- and low-speed streak pairs was only one; how-
75 ever, the turbulent structure was maintained. The mean streak spacing was always comparable to that of the flat plate. In addition, there are many investigations of uncontrolled turbulent flow along a thin cylinder. However, a control aiming to decrease the skin-friction drag has not yet been examined for turbulent flows along a cylinder.

80 In the present study, we performed the DNS in turbulent flow along the cylinder with opposition control and investigated the influence of the transverse curvature on the drag reduction effect. For turbulent flow control, we employed a classical opposition control technique (i.e., the so-called v -control, Choi *et al.* [1])

for the sake of simplicity. Seven curvatures and six detection plane heights were
85 investigated at the same Reynolds number. In addition to the drag reduction
effect, we also investigated the relationship between the turbulent statistics and
drag reduction rate, and the mechanism based on energy transport analysis.

2. Direct Numerical Simulation

We performed the DNS of the turbulent flow along the cylinder. The governing equations are incompressible continuity equation and Navier-Stokes equations in a cylindrical coordinate system. The continuity equation is

$$\frac{1}{r} \frac{\partial}{\partial r}(ru_r) + \frac{1}{r} \frac{\partial u_\theta}{\partial \theta} + \frac{\partial u_z}{\partial z} = 0, \quad (3)$$

where u is the velocity and r , θ , and z represent the radial, azimuthal, and axial directions, respectively. The Navier-Stokes equations are

$$\frac{\partial u_r}{\partial t} = -h_r - \frac{\partial p}{\partial r} + \frac{1}{\text{Re}_b} d_r, \quad (4)$$

$$\frac{\partial u_\theta}{\partial t} = -h_\theta - \frac{1}{r} \frac{\partial p}{\partial \theta} + \frac{1}{\text{Re}_b} d_\theta, \quad (5)$$

$$\frac{\partial u_z}{\partial t} = -h_z - \frac{\partial p}{\partial z} - \frac{\partial P}{\partial z} + \frac{1}{\text{Re}_b} d_z. \quad (6)$$

Here, t is the time, p is the pressure, h is the convection terms, and d is the diffusion term. The mean pressure gradient $-\frac{\partial P}{\partial z}$ is a driving force. The convection and diffusion terms are given by

$$h_r = \frac{1}{r} \frac{\partial}{\partial r}(ru_r u_r) + \frac{1}{r} \frac{\partial}{\partial \theta}(u_\theta u_r) + \frac{\partial}{\partial z}(u_z u_r) - \frac{u_\theta^2}{r}, \quad (7)$$

$$h_\theta = \frac{1}{r} \frac{\partial}{\partial r}(ru_r u_\theta) + \frac{1}{r} \frac{\partial}{\partial \theta}(u_\theta u_\theta) + \frac{\partial}{\partial z}(u_z u_\theta) + \frac{u_r u_\theta}{r}, \quad (8)$$

$$h_z = \frac{1}{r} \frac{\partial}{\partial r}(ru_r u_z) + \frac{1}{r} \frac{\partial}{\partial \theta}(u_\theta u_z) + \frac{\partial}{\partial z}(u_z u_z), \quad (9)$$

$$d_r = \frac{1}{r} \frac{\partial}{\partial r} \left(r \frac{\partial u_r}{\partial r} \right) - \frac{u_r}{r^2} + \frac{1}{r^2} \frac{d^2 u_r}{d\theta^2} + \frac{d^2 u_r}{dz^2} - \frac{2}{r^2} \frac{\partial u_\theta}{\partial \theta}, \quad (10)$$

$$d_\theta = \frac{1}{r} \frac{\partial}{\partial r} \left(r \frac{\partial u_\theta}{\partial r} \right) - \frac{u_\theta}{r^2} + \frac{1}{r^2} \frac{d^2 u_\theta}{d\theta^2} + \frac{d^2 u_\theta}{dz^2} + \frac{2}{r^2} \frac{\partial u_r}{\partial \theta}, \quad (11)$$

$$d_z = \frac{1}{r} \frac{\partial}{\partial r} \left(r \frac{\partial u_z}{\partial r} \right) + \frac{1}{r^2} \frac{d^2 u_z}{d\theta^2} + \frac{d^2 u_z}{dz^2}. \quad (12)$$

The reference velocity and length are twice the bulk velocity $2u_b^*$ and the boundary layer thickness δ^* , respectively. The DNS code is based on that by Fukagata *et al.* [16]: the governing equations are spatially discretized using the finite-difference method with a second-order central differencing scheme (Ham *et al.* [17]). Further, the second-order Crank-Nicolson scheme is employed for

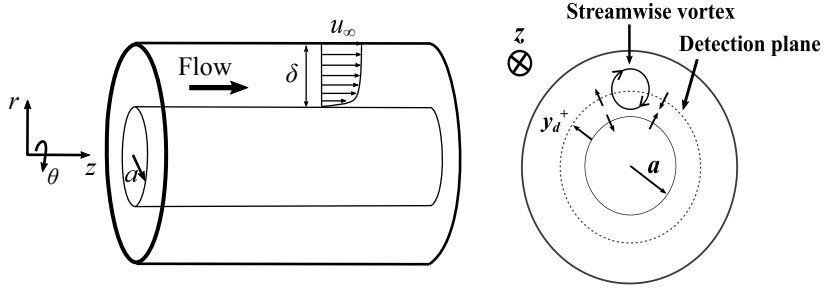


Figure 1: Schematic of opposition controlled flow along a thin cylinder.

the viscous terms and low-storage third-order Runge-Kutta scheme is employed
 95 for the other terms (Spalart *et al.* [18]).

Figure 1 shows a schematic of opposition controlled turbulent flow along a
 cylinder. The computational domain size is $L_z^+ \approx 4000$ in the axial direction
 and $\delta = 1$ in the radial direction. Non-uniform spaced grids are used only
 in the radial direction, and the number of grid points is $N_r \times N_\theta \times N_z =$
 100 $96 \times 128 \times 320$. The curvature ratio of γ are six cases from 2 to 17. For
 comparison, the turbulent channel flow is also simulated as $\gamma = 0$. In the present
 channel flow case, the DNS code is based on that by Fukagata *et al.* [19], the
 computational domain is set to $L_x \times L_y \times L_z = 4\pi \times 2 \times 2\pi$ in the streamwise,
 wall-normal, and spanwise direction, respectively. The number of grid points is
 105 $N_x \times N_y \times N_z = 256 \times 192 \times 256$, and the skin-friction Reynolds number of Re_τ ,
 based on the half channel width and wall-friction velocity, is set to 180. The
 bulk Reynolds number of Re_b is set to 5700–6580 for $\gamma = 0$ –17 so that the free-
 stream Reynolds number of Re_δ based on the boundary layer thickness and the
 free-stream velocity is approximately 3400. Details of the mean flow parameters
 110 are shown in Table 1. Here, the superscript “+” indicates the wall units, a is
 the cylinder radius, and $C_{f,\infty} = 2\tau_w^*/\rho^*u_\infty^{*2}$ is the skin-friction coefficient.

The periodic condition is imposed in the axial direction. At the outer bound-
 ary of the computational domain, we imposed zero stress condition as,

$$\frac{\partial}{\partial r} \left(\frac{u_\theta}{r} \right) = 0, \quad \frac{\partial u_z}{\partial r} = 0, \quad u_r = 0. \quad (13)$$

On the cylinder surface, a no-slip condition is employed in the uncontrolled case,

Table 1: Uncontrolled flow parameters employed in the present study

$\gamma = \delta^*/a^*$	L_z	L_z^+	Re_b	Re_τ	Re_δ	a^+	$C_{f,\infty}$
0	4π	2237	5700	180	3330	—	5.90×10^{-3}
2	6.4π	3979	6200	198	3380	99	6.04×10^{-3}
5	6π	4012	6400	213	3390	42	7.84×10^{-3}
8	5.7π	4044	6480	226	3400	28	8.80×10^{-3}
11	5.4π	4018	6500	237	3380	22	9.80×10^{-3}
14	5.2π	4033	6500	247	3370	18	10.72×10^{-3}
17	5π	4066	6580	259	3400	15	11.59×10^{-3}

whereas the wall-velocity is applied in the controlled cases as

$$u_{r,w}(\theta, z, t) = -u_r(y_d^+, \theta, z, t). \quad (14)$$

$u_{r,w}$ corresponds to the v -control as suggested by Choi *et al.* [1], and y_d^+ is the location of the detection plane. In the computational procedure, the control input is based on the velocity distribution detected in the previous time step.

115 Here, y_d^+ is normalized by the uncontrolled wall-friction velocity. We examine the radial u_r -control with six different detection planes ($y_d^+ = 5$ -30).

All the simulations start from a fully developed turbulent flow along the thin cylinder. As the flow rate in the axial direction is kept constant, the drag reduction effect corresponds to a decrease in the wall shear stress. By integrating the kinetic energy equation temporally and spatially, the energy balance of the entire system can be expressed as follows:

$$\underbrace{\left[-u_z \frac{\partial P}{\partial z} \right]_T}_{W_p} + \frac{2a}{2a+1} \underbrace{\left\langle \left(u_r p' + \frac{1}{2} u_r^3 \right)_w \right\rangle_T}_{W_a} = \frac{1}{\text{Re}_b} [\varepsilon]_T. \quad (15)$$

In this study, the averaging operators of $\langle \rangle$ and $[\]$ denote the uniform-spatial

(in θ - and z - directions) and volume average, respectively:

$$\begin{aligned}\langle\phi\rangle(r,t) &= \frac{1}{2\pi L_z} \int_0^{L_z} \int_0^{2\pi} \phi(r,\theta,z,t) d\theta dz, \\ [\phi](t) &= \frac{2}{2a+1} \int_a^{a+1} \langle\phi\rangle(r,t) r dr.\end{aligned}\tag{16}$$

Here, ε is the viscous dissipation, W_a is the pumping power, W_p is the actuation power, $\phi(r,\theta,z,t)$ is an arbitrary variable, and the subscript “ T ” (e.g., $\langle\phi\rangle_T$) represents the temporal average. The cost functions are the drag reduction rate R_D , the net energy saving rate S , and the energy gain G , as

$$\begin{aligned}R_D &= \frac{W_{p0} - W_p}{W_{p0}}, \\ S &= \frac{W_{p0} - (W_p + W_a)}{W_{p0}}, \\ G &= \frac{W_{p0} - (W_p + W_a)}{W_a},\end{aligned}\tag{17}$$

respectively. The subscript ‘0’ shows the uncontrolled flow. Since the flow rate is constant, R_D is equal to the reduction rate of the wall shear stress.

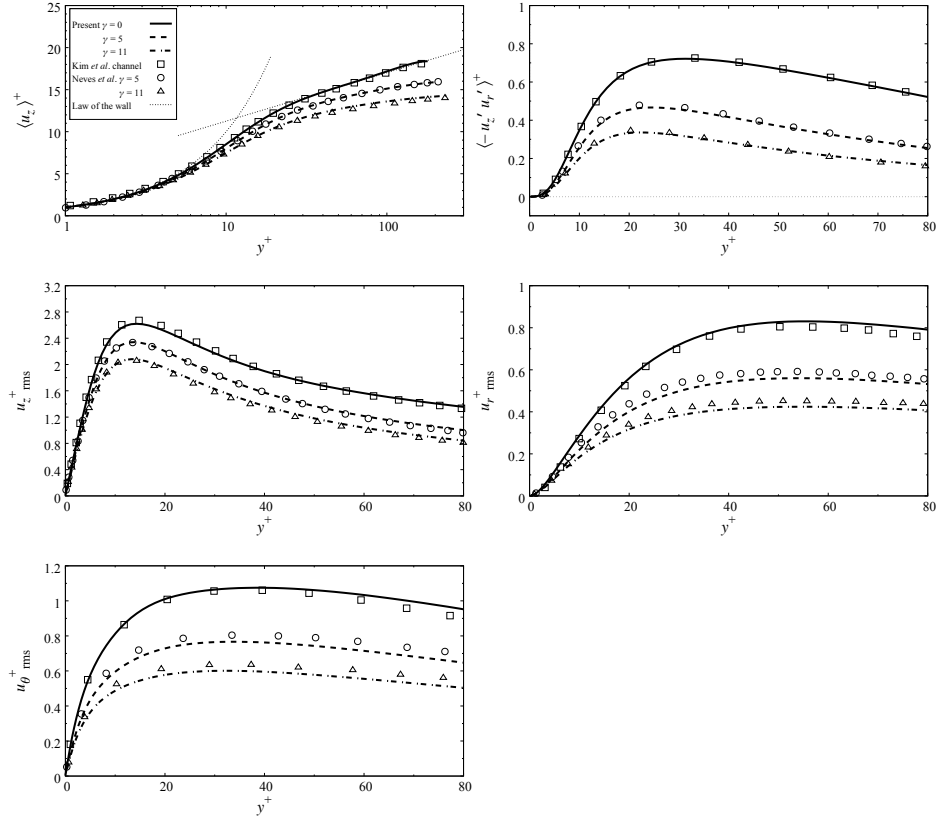


Figure 2: Turbulent statistics as compared with that of Neves *et al.* [9] and Kim *et al.* [20].

As shown in Fig. 2, statistics of uncontrolled flow in the present DNS are compared with those of Kim *et al.* [20] and Neves *et al.* [9]. The cylinder radius a^+ and cylinder curvature γ are set to be comparable to those of them. All statistics decrease with increasing curvature, which is in good agreement with the references.

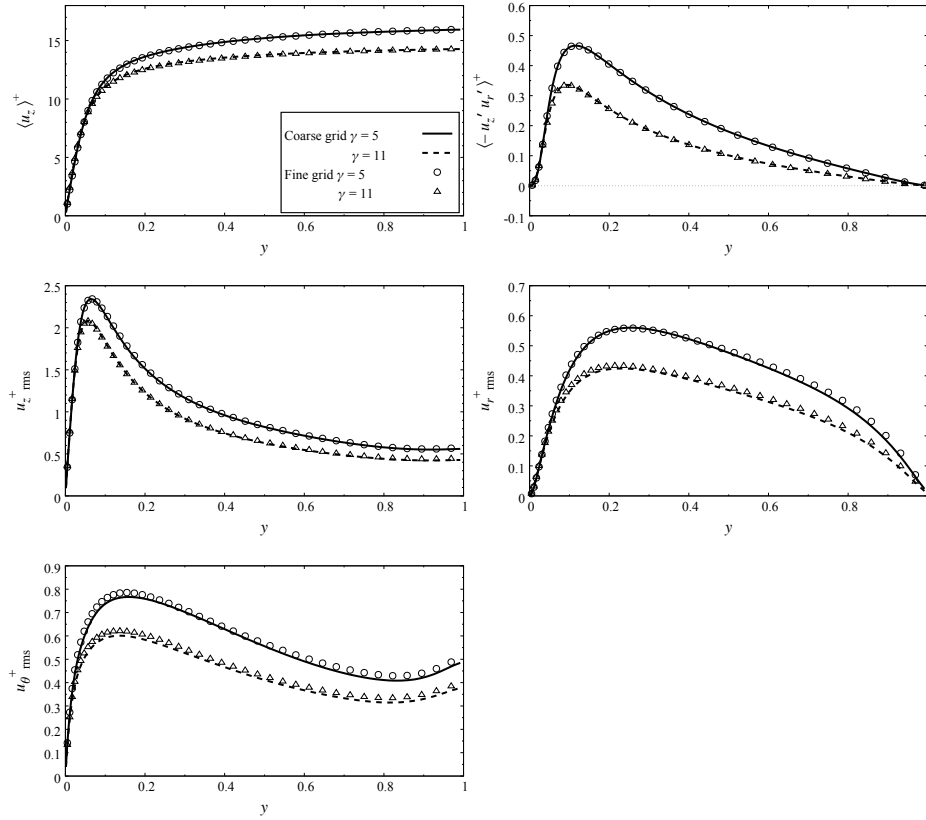


Figure 3: Grid number dependence of turbulence statistics.

To verify the grid dependency, calculations are performed with $N_r \times N_\theta \times$
 125 $N_z = 128 \times 256 \times 512$ as a fine grid. A coarse grid means $N_r \times N_\theta \times N_z = 96 \times$
 128×320 . For $\gamma = 5$, the grid spacings of a fine grid are $\Delta z^+ = 7.8$, $(r\Delta\theta)^+ = 1-$
 6.3 , and $\Delta r^+ = 0.4-2.5$. Figure 3 shows the grid number dependency of the
 turbulent statistics. The turbulent statistics are in good agreement with those
 of the coarse grid case.

130 3. Results and Discussion

3.1. Control efficiency

Figure 4 shows the drag reduction rate R_D , the net energy saving rate S , and the energy gain G as a function of the detection plane height y_d^+ . Figure 4(b), (d), and (f) correspond to the enlarged view of Fig. 4(a), (c), and (e), respectively. As shown in Fig. 4(b), the drag reduction rate peaks at $y_d^+ = 15$ in all cases except $\gamma = 11$, while these are smaller than those in the case of $\gamma = 0$: the maximum drag reduction rate by the v -control was about $R_D = 25\%$ (present DNS and Choi *et al.* [1]). As increasing the height of the detection plane, the drag reduction rate decreases for both channel flow and flow along a cylinder. However, in the cases of $\gamma \geq 11$, a positive drag reduction rate is obtained even at $y_d^+ = 30$. It implies that the drag reduction effect can be achieved at a higher detection plane in the large curvature case. A comparison of the drag reduction rate and the net energy saving rate in Fig. 4(c) shows that actuation power is extremely small at $y_d^+ \leq 20$ because of the similar distribution. At $y_d^+ \geq 25$, as the magnitude of the actuation power increases, the net energy saving rate is further reduced compared to the drag reduction rate. As the curvature decreases, the difference from the drag reduction rate increases. As shown in Fig. 4(e), the energy gain summits at approximately $y_d^+ = 10$ –15. In addition, in the case where the wall has a transverse curvature, the energy gain is higher than that in the case of $\gamma = 0$.

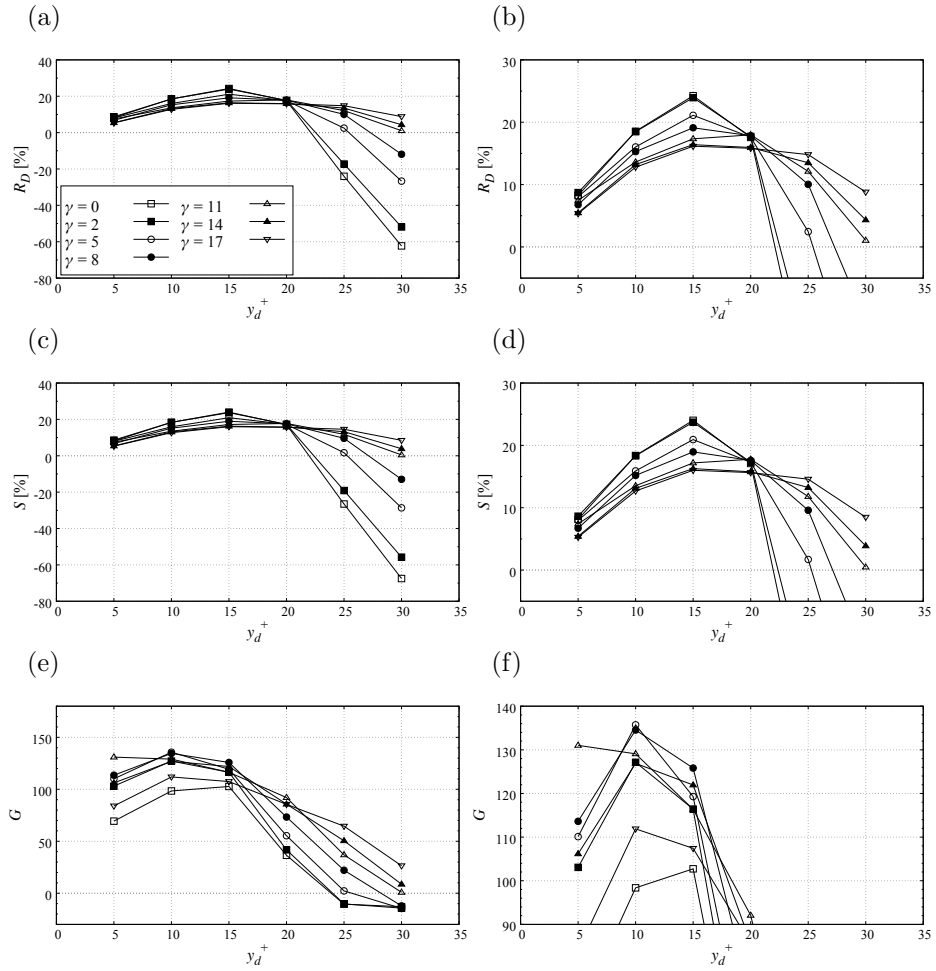


Figure 4: Distributions of the (a-b) drag reduction rate, (c-d) net energy saving rate, and (e-f) energy gain as a function of the detection plane height. (b), (d), and (f) denote the enlarged view of (a), (c), and (e), respectively.

3.2. Turbulent statistics

Figure 5 shows turbulent statistics at $y_d^+ = 15$. All variables are normalized by the uncontrolled wall-friction velocity $u_{\tau 0}$. As shown as Fig. 5(a), in the uncontrolled case, the mean axial velocity in the buffer layer ($5 < y^+ < 30$) and the log-law region ($y^+ > 30$) decreases with an increase in the cylinder curvature (Neves *et al.* [9]). In both controlled cases, the mean velocity in the viscous sublayer ($y^+ < 5$) and the buffer layer decreases, whereas there is no change in the log-law region, which is a similar trend to that in the controlled channel flow. As shown in Fig. 5(b)-(e), the Reynolds shear stress (RSS, $\langle -u'_z u'_r \rangle$) and the rms values of the velocities decrease with increasing curvature (Neves *et al.* [9]). It is found that the trend of the control effect is similar to that in the channel flow: the rms values of the velocities and the RSS decrease in most of the region. Because the RSS plays an important role in the skin-friction coefficient, a reduction in the RSS contributes to a decrease in the skin-friction coefficient (Fukagata *et al.* [14] and Monte *et al.* [13]). Moreover, a local minimum of the RSS and $u_{r \text{ rms}}^+$ is established between the cylinder wall and the detection plane. The location of the local minimum is known as the virtual wall (Hammond *et al.* [2]). As compared with the channel flow case ($\gamma=0$), the virtual wall approaches to the wall in the case of $\gamma=11$ because of the difference in the friction Reynolds number. As presented in Fig. 5(f)-(h), although the rms values of vorticities also decrease with increasing curvature, quasi-stream vortices exist near the wall (Ohta [15]). In the Rankine vortex model, the mean radius of streamwise vortices is estimated from the distance between the peak and valley positions of $\omega_z^+_{\text{rms}}$ and the strength is defined by the peak value of it. Under the uncontrolled flow, the mean radius is smaller than that in the case of $\gamma = 0$. However, regardless of the curvature, the peak and valley positions of $\omega_z^+_{\text{rms}}$ shift outward after control, and the mean radius is slightly larger than that in the uncontrolled case. Furthermore, the strength defined by the peak value of $\omega_z^+_{\text{rms}}$ is greatly attenuated by the control and the decrement in the channel flow is larger than that in $\gamma = 11$. The maximum positions of $\omega_r^+_{\text{rms}}$ move outward, which indicates that the streaks are kept away from the

wall (Wang *et al.* [6]). Furthermore, $\omega_{r\text{ rms}}^+$ is distributed on the same linear line near the wall regardless of the control.

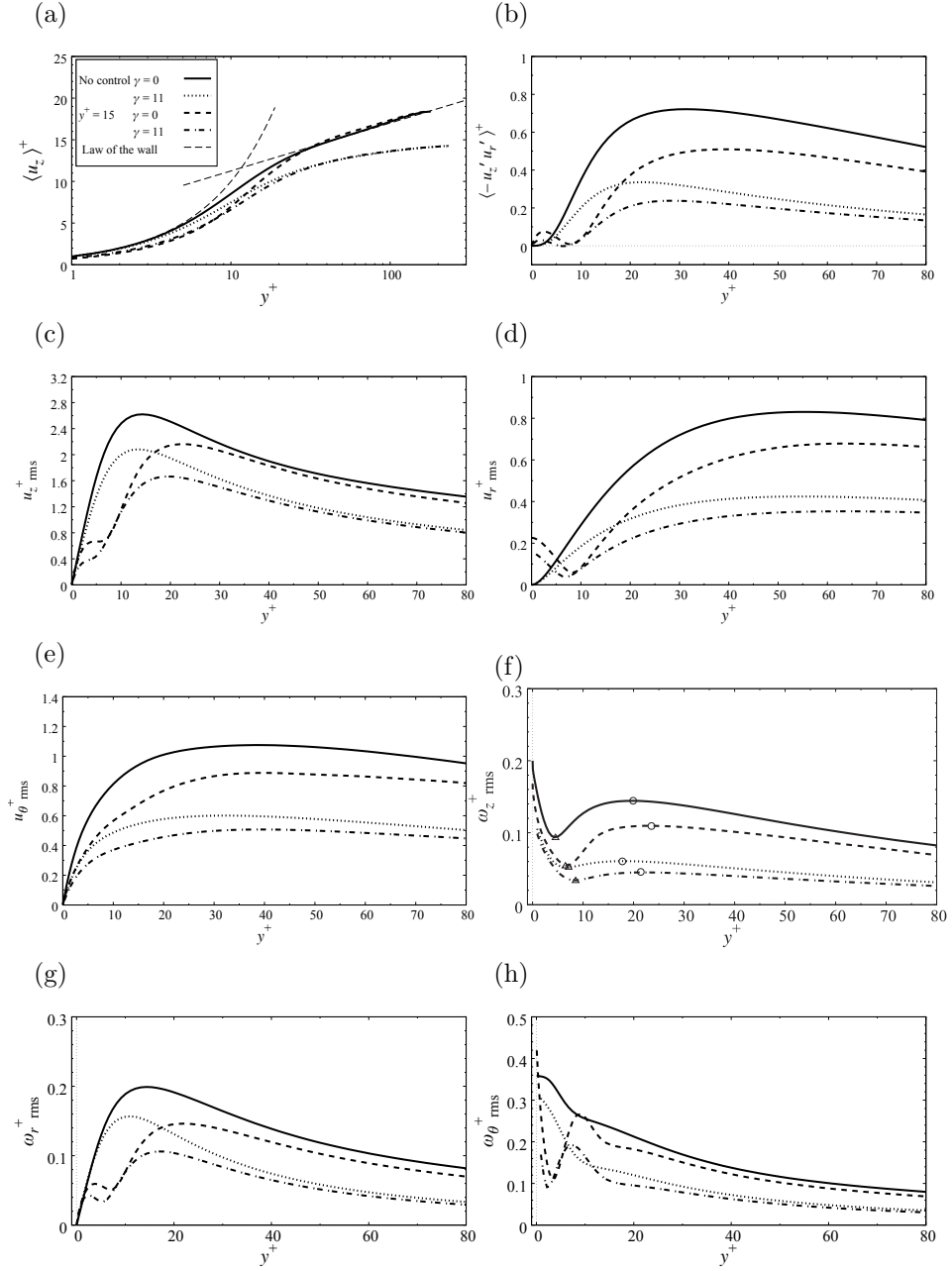


Figure 5: Turbulent statistics at $y_d^+ = 15$. All variables are normalized by the uncontrolled wall-friction velocity. For $\omega_{z, \text{rms}}^+$, local maximum and minimum peaks are denoted by \circ and \triangle , respectively.

Figure 6 shows turbulent statistics at $y_d^+ = 25$. It is seen in Fig. 6(a) that
185 the mean axial velocity in the viscous sublayer and the buffer layer decreases for
both curvature cases, and the decrement after control is slightly larger than that
at $y_d^+ = 15$. As shown in Fig. 6(b)-(e), in the buffer region, the RSS and the
rms values of the velocities decrease by control at $\gamma = 11$, while they increase in
the channel flow. The peak position of $u_z^+_{\text{rms}}$ corresponds to the position where
190 high- and low-speed streaks appear most often. In the channel flow, the peak
value hardly changes, and the peak position shifts toward the wall, indicating
that the wall shear stress increases. When the drag is reduced, the peak value
is much smaller than that in the uncontrolled case, and the peak position moves
away from the wall. A local minimum of $u_r^+_{\text{rms}}$ is established for all the control
195 cases, demonstrating that the virtual wall is formed independently of increasing
or decreasing the drag. It can also be seen in Fig. 6(f)-(h) that the distribution
of $\omega_z^+_{\text{rms}}$ increases greatly in the channel flow, while it hardly changes at $\gamma = 11$.
The valley of $\omega_z^+_{\text{rms}}$ shifts outward for both curvature. However, the peak shifts
toward the wall and outward for the channel flow and $\gamma = 11$, respectively.
200 In addition, the peak increases significantly in the channel flow, while it is
unchanged in $\gamma = 11$. The distribution of $\omega_r^+_{\text{rms}}$ increases and decreases with
respect to the cases of $\gamma = 0$ and $\gamma = 11$, respectively. At $y_d^+ = 15$, $\omega_r^+_{\text{rms}}$ is
distributed on the same linear line near the wall as in the uncontrolled case.
However, at $y_d^+ = 25$, the linear lines distributed are different, and the gradient
205 is steep.

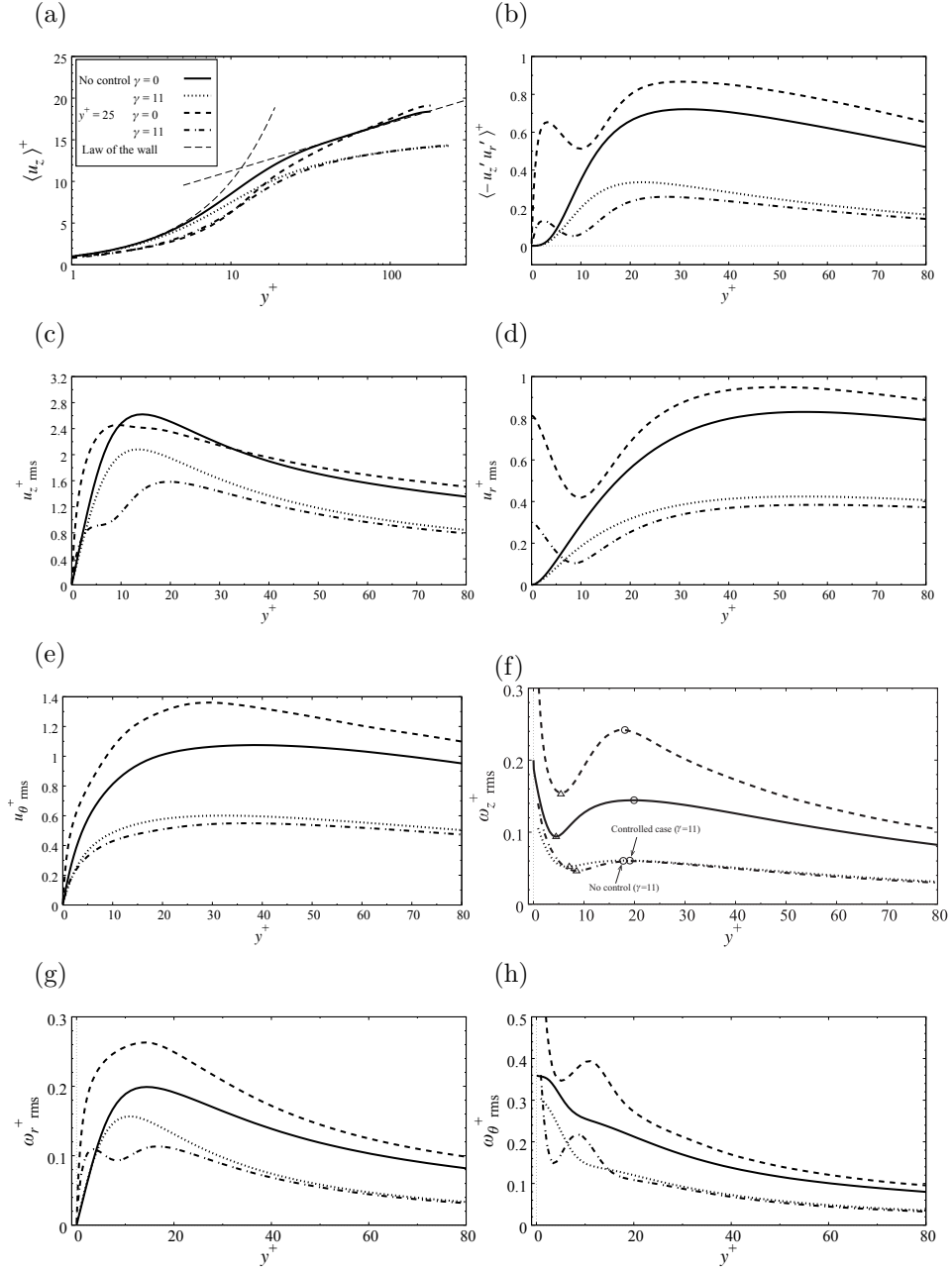


Figure 6: Turbulent statistics at $y_d^+ = 25$. All variables are normalized by the uncontrolled wall-friction velocity. For $\omega_{z,rms}^+$, local maximum and minimum peaks are denoted by \circ and \triangle , respectively.

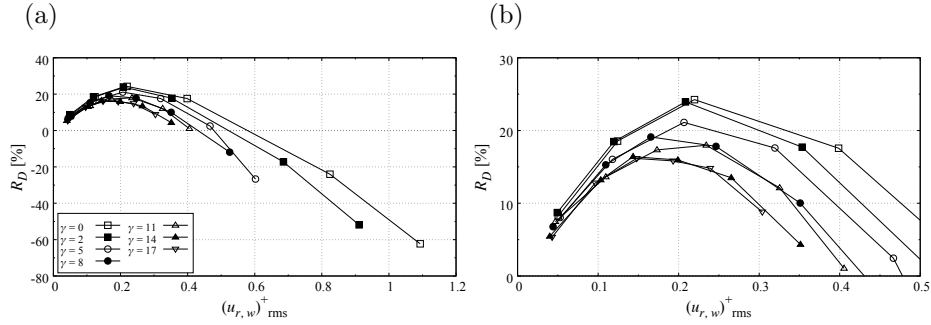


Figure 7: Drag reduction rate and rms values of the radial velocity on the wall: (a) over view, (b) enlarged view of positive drag reduction rate. The value of $(u_{r,w})_{rms}^+$ is normalized by the uncontrolled wall-friction velocity.

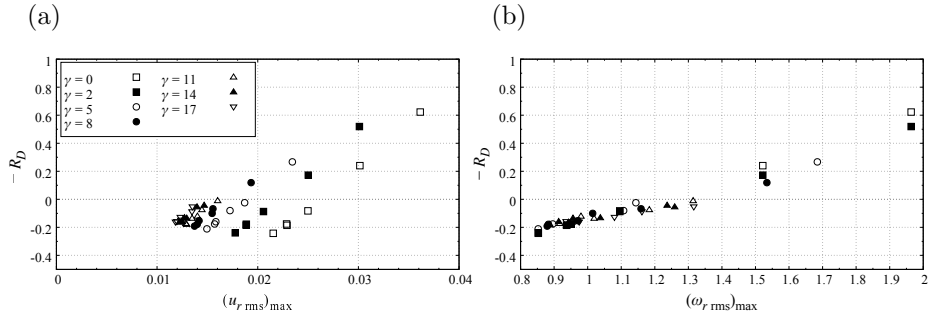


Figure 8: Correlation between the negative drag reduction rate $-R_D$ and the peak value of (a) the radial turbulence intensity and (b) the radial vorticity intensity. The values of $(u_{r,rms})_{max}$ and $(\omega_{r,rms})_{max}$ are normalized by $2u_b^*$ and δ^* .

Figure 7 is showing the rms value of $u_{r,w}$ and the drag reduction rate for all the cases. Figure 7(b) corresponds to the enlarged view of Fig. 7(a). When the curvatures are different, the rms values of $u_{r,w}$ also differ greatly even at the same detection plane height. However, the peak value of R_D at each curvature is in the range of $0.15 \leq (u_{r,w}^+)_{rms} \leq 0.25$. For $(u_{r,w}^+)_{rms} < 0.15$, the correlation generally follows $R_D \sim 1.5(u_{r,w}^+)_{rms}$. These trends are observed regardless of the curvature.

Figure 8 shows the correlation between the drag reduction rate, peak value of $u_{r,rms}$, and $\omega_{r,rms}$. The maximum values of $u_{r,rms}$ and $\omega_{r,rms}$ are strongly correlated with the drag reduction rate. Chung *et al.* [3] reported that these

are distributed on the same linear line regardless of the strength of blowing and suction. However, in the present case, the peak values of $u_{r \text{ rms}}$ are distributed on a different linear line for each curvature, indicating that the influence of the curvature on control efficiency cannot be discussed only by the difference in the strength of blowing and suction. On the other hand, all of the peak values of $\omega_{r \text{ rms}}$ are distributed on one linear line only when $\omega_{r \text{ rms}}$ is normalized by the $2u_b$ and ν . In particular, there is a strong linear relationship in a range of $-R_D < 0$.

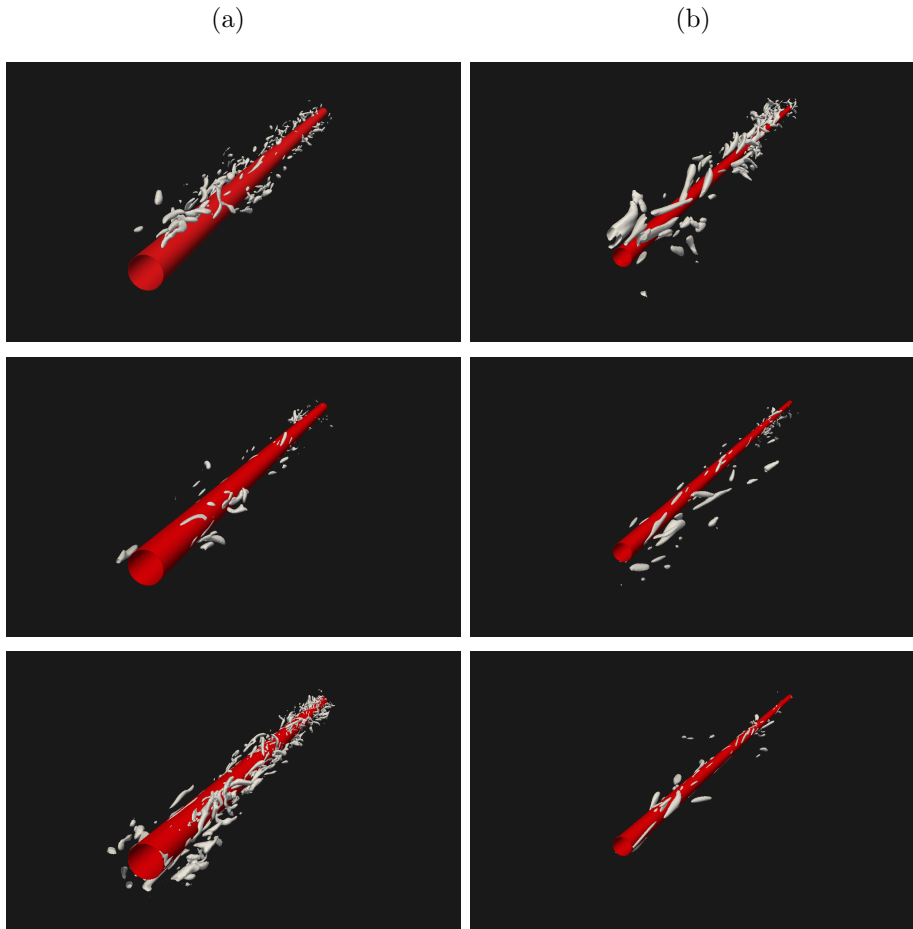


Figure 9: Instantaneous vortical structure defined by the isosurface of the second invariant of the velocity gradient tensor at (a) $\gamma = 5$ at $Q^+ = 0.01$ and (b) $\gamma = 11$ at $Q^+ = 0.004$: (top row) no control, (middle row) $y_d^+ = 15$, (bottom row) $y_d^+ = 25$.

3.3. Visualization of flow field

225 Figure 9 shows the instantaneous visualization of the vortical structure in
the case of $\gamma = 5$ and 11. Here the vortical structure is defined by the isosur-
face of the second invariant of the velocity gradient tensor. Since the vorticity
intensity decreases as the curvature increases, the vortical structure is not de-
tected or is excessively detected if the same isosurface value is used. Therefore,
230 the isosurface values are set to $Q^+ = 0.01$ and 0.004 for $\gamma = 5$ and 11, respec-

tively. Firstly, focusing on the case of $\gamma = 5$, the vortical structure at $y_d^+ = 15$ is significantly suppressed compared to the uncontrolled case, indicating that the high drag reduction rate is qualitatively obtained by the control. On the other hand, at $y_d^+ = 25$, the same amount of vortical structure is observed as the uncontrolled case, indicating that the drag reduction effect is lower than at $y_d^+ = 15$. Choi *et al.*[1] and Hammond *et al.*[2] reported that the vortical structure increases when the detection plane is far away from the wall, and the visualization of $\gamma = 5$ in the present study shows a similar tendency. Next, paying attention to the case of $\gamma = 11$, the vortical structure is significantly reduced in both cases of $y_d^+ = 15$ and 25 compared to the uncontrolled case. This is different from the case of small curvature such as channel flow and $\gamma = 5$. From these results, it is found that in the case of high curvature, the high drag reduction effect is obtained even on the distant detection plane.

Figure 10 shows the instantaneous axial velocity fluctuations and velocity vectors in the $r - \theta$ plane at $\gamma = 5$ and 11. As shown in Fig. 2, since the increase in the cylinder curvature weakens the turbulence intensity, the axial velocity fluctuations in case of $\gamma = 11$ are smaller than those in case of $\gamma = 5$. At $y_d^+ = 15$, the streaks are separated from the wall compared to the uncontrolled case regardless of the curvature, and the vortical structure is suppressed. Moreover, there are no streaks inside the virtual wall. Focusing on the case of $\gamma = 5$ and $y_d^+ = 25$, streaks exist inside the virtual wall, and the vortical structure near the wall is promoted. On the other hand, in the case of $\gamma = 11$ and $y_d^+ = 25$, the trend is similar to the result of $y_d^+ = 15$. These results show that when the streaks do not exist inside the virtual wall, significant suppression of the vortical structure is obtained.

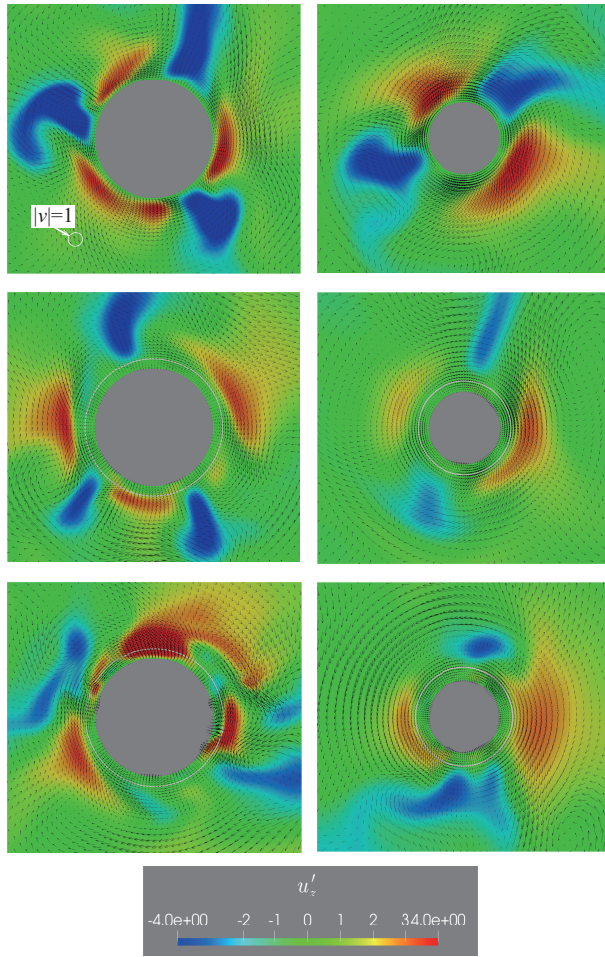


Figure 10: Contours of axial velocity fluctuations normalized by the uncontrolled wall-friction velocity and velocity vectors of (u_r, u_θ) in the $r - \theta$ plane of the instantaneous at (left) $\gamma = 5$ and (right) $\gamma = 11$: (top row) no control, (middle row) $y_d^+ = 15$, (bottom row) $y_d^+ = 25$. White line denotes the virtual wall defined as a local minimum of u_r rms.

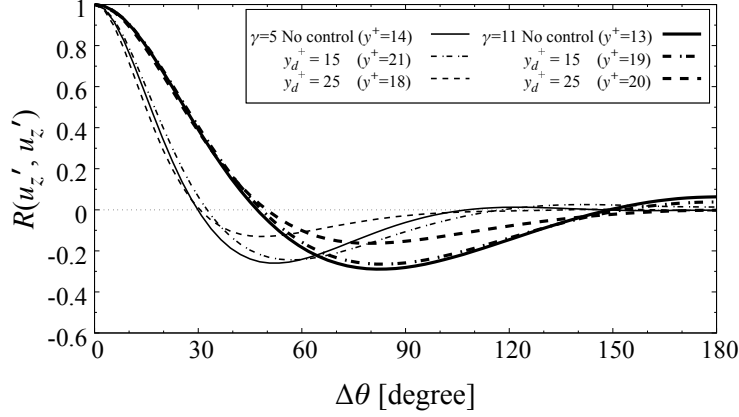


Figure 11: Azimuthal two-point correlation of the axial velocity fluctuation at the peak position of u_z rms. In the legend box, y^+ means the peak location of u_z rms.

Figure 11 shows the azimuthal two-point correlation of the axial velocity $R(u'_z, u'_z)$ at the peak position of u_z rms. The minimum peak of $R(u'_z, u'_z)$ corresponds a space of streaky structures of the velocity. Focusing on the case of $\gamma = 5$, the local minimum of $R(u'_z, u'_z)$ is at 50° , indicating that three or four pairs of the streaky structures exist. In the case of $\gamma = 11$, since the local minimum is at 80° , there are two or three pairs. However, because the two-point correlation is almost unchanged in the control cases, the control does not affect the number of pairs of the streaky structures, which is similar to that in channel flow (Choi *et al.*[1]). The number of pairs is unchanged in the controlled flow, which is consistent with Fig. 10.

3.4. Contribution to skin-friction coefficient

Investigations on the drag reduction mechanism in the turbulent flow along the cylinder are performed and compared with those in the channel flow. According to the report by Monte *et al.* [13], the skin-friction coefficient is identical to the sum of the three terms (contributions of the inhomogeneous and the transient are negligible) as follows:

$$f(a)C_{f,\infty} = (a+1) \int_a^{a+1} \frac{1}{\text{Re}_\delta} \frac{\partial \langle u_z \rangle_T}{\partial r} r dr - \frac{(\delta^* + a)^2}{\text{Re}_\delta} + \int_a^{a+1} (a+1-r) \langle -u'_z u'_r \rangle_T r dr. \quad (18)$$

Here, all variables are normalized by the free-stream velocity u_∞^* and the boundary layer thickness δ^* , $f(a)$ is the shape factor of the cylindrical geometry, δ^* is the displacement thickness, these variables are defined by

$$f(a) = \frac{a}{4} - \frac{a}{2a+1} \left(\frac{1}{24} + \frac{a}{6} \right),$$

$$(a + \delta^*)^2 - a^2 = 2 \int_a^{a+1} \left(1 - \frac{\langle u_z \rangle_T}{u_\infty} \right) r dr. \quad (19)$$

Since $f(a)$ is approximately equal to a linear distribution, $f(a)$ decreases at large curvatures (i.e., small radius). The shape factor is the unique variable in the turbulent flow along the cylinder, and does not appear in the identity of the channel flow and the boundary layer flow.

270

Figure 12 shows the cumulative contributions to the skin-friction coefficient. Here, cumulative contributions are defined as,

$$\begin{aligned}
C_f^W(r) &= \frac{1+a}{f(a)} \int_a^r \frac{1}{\text{Re}_\delta} \frac{\partial \langle u_z \rangle_T}{\partial r} r dr, \\
C_f^D &= -\frac{1}{f(a)} \frac{(\delta^* + a)^2}{\text{Re}_\delta}, \\
C_f^T(r) &= \frac{1}{f(a)} \int_a^r (1+a-r) \langle -u'_z u'_r \rangle_T r dr,
\end{aligned} \tag{20}$$

respectively, i.e., the sum of contributions at $y = 1$ (i.e., $r = a+1$) is equal to the C_f . Focusing on the uncontrolled value at $y = 1$, C_f^D is about -1.0×10^{-3} for all curvatures. When C_f^D and C_f^T at $\gamma = 17$ are compared with those in the case of $\gamma = 5$, increases of about 1.0×10^{-3} and 3.0×10^{-3} are observed, respectively. Therefore, the skin-friction coefficient increases as the curvature increases due to the increase in C_f^D and C_f^T . Focusing on the change in contributions due to the control, contributions of C_f^W and C_f^D are not affected regardless of the curvature. Therefore, only the contribution of C_f^T affects the change in the skin-friction coefficient. In fact, in case where the high drag reduction rate is obtained (for example, $\gamma = 5$ and $y_d^+ = 15$), C_f^T is greatly reduced. Moreover, since C_f^T is equivalent to the integration of weighted RSS, the decrease in RSS is strongly related to the reduction in drag. Here, we compare it to the channel flow. The identity in channel flow is given by

$$C_{f,b} = \frac{12}{\text{Re}_b} + 12 \int_0^1 2(1-y) \langle -u'v' \rangle_T dy. \tag{21}$$

In the channel flow, when the second term is reduced by the opposition control, the drag reduction effect can be obtained (Fukagata *et al.*[14]). From the above results, it is evident that with the channel flow, only the term related to RSS is affected by the control.

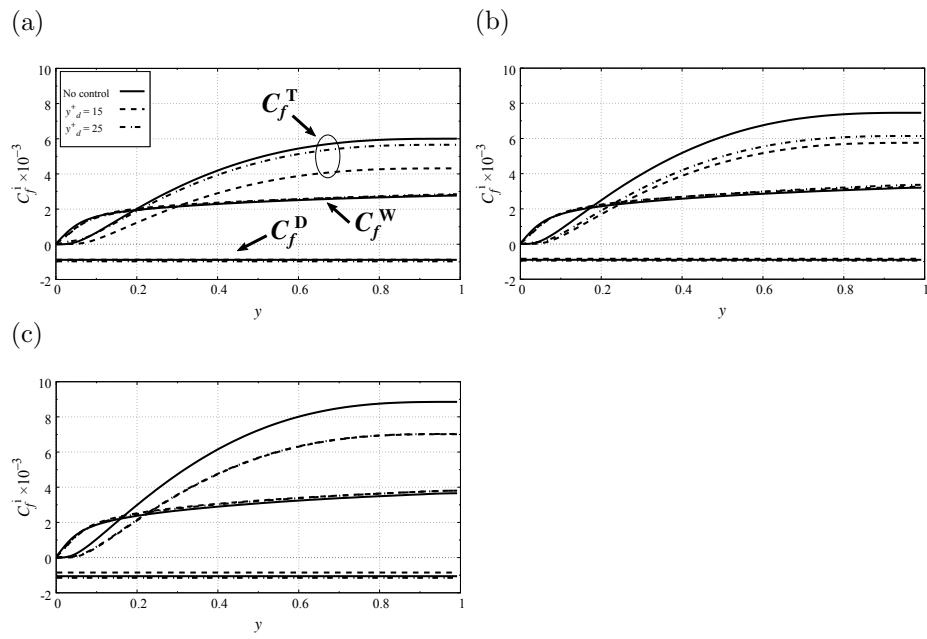


Figure 12: Cumulative contributions to skin-friction coefficient: (top) $\gamma = 5$, (middle) $\gamma = 11$, (bottom) $\gamma = 17$.

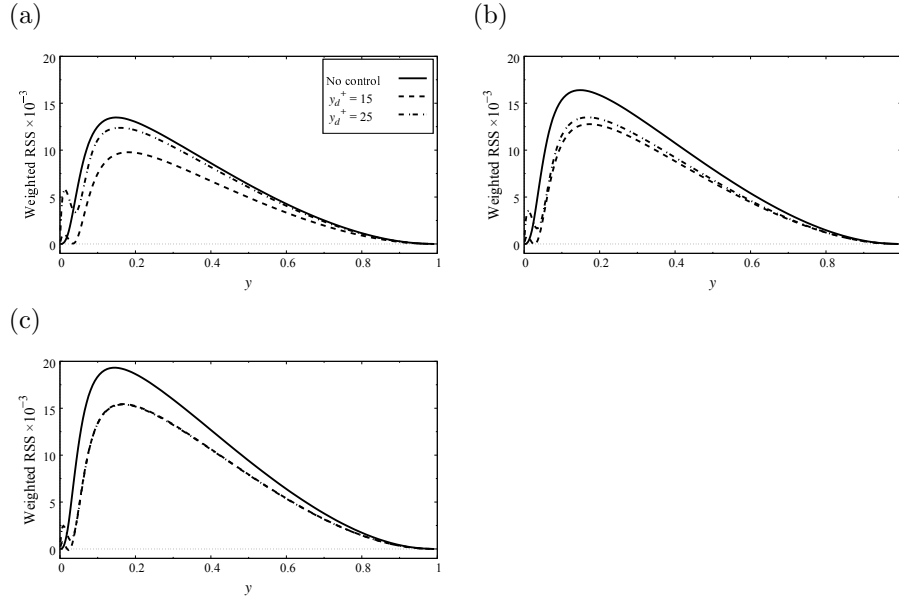


Figure 13: Distributions of the weighted Reynolds shear stress: (a) $\gamma = 5$, (b) $\gamma = 11$, (c) $\gamma = 17$.

275 The weighted RSS is shown in Fig. 13. Here, weighted RSS is the integral
function of C_f^T including $f(a)$. In contrast to the distribution of the RSS, with
an increase in the curvature, the weighted RSS increases because $f(a)$ decreases,
and it causes an increase in the skin-friction coefficient. In the controlled cases,
since the blowing and suction create the RSS in the region near the wall, the
280 small peak appears. In the case of $\gamma = 5$, the increment at $y_d^+ = 25$ cancels out
the decrement of the weighted RSS; it results in the small drag reduction rate.
Contrarily, in the cases of $\gamma \geq 11$, the increment at $y_d^+ = 25$ of the weighted
RSS in the region near the wall is smaller than the decrement of the weighted
RSS. Therefore, the drag reduction effect can be obtained at a higher detection
285 plane.

3.5. Temporal variation of Reynolds stress

The analysis of the contribution to the skin-friction coefficient reveals that in the turbulent flow along the cylinder, the term related to the RSS such as the channel flow, is affected by the opposition control. Therefore, change in RSS is strongly related to change in the skin-friction coefficient. Based on these facts, the changing process of the RSS is investigated from the analysis of energy transport. Immediately after the start of the opposition control, the energy balance may not be balanced due to the strong blowing and suction from the wall (Ge *et al.*[5]). In this study, by introducing temporal relaxation for the control strength, a sudden change in physical quantity near the wall is mitigated, and energy imbalance is avoided. The control formula is given by

$$u_{r,w}(\theta, z, t) = -u_r(y_d^+, \theta, z, t)(1 - e^{-(t/\mathcal{T})^2}). \quad (22)$$

Here, \mathcal{T} is the relaxation time and it is set at $\mathcal{T} = 500$. This formula is the same as that used by Ge *et al.*[5]. The larger the \mathcal{T} , more slowly the strength of blowing and suction converges. When about $3\mathcal{T}$ is elapsed since the start
290 of the control, the difference between the original control and the time-relaxed control is almost negligible. (The relaxation time \mathcal{T} is not introduced in the earlier sections.)

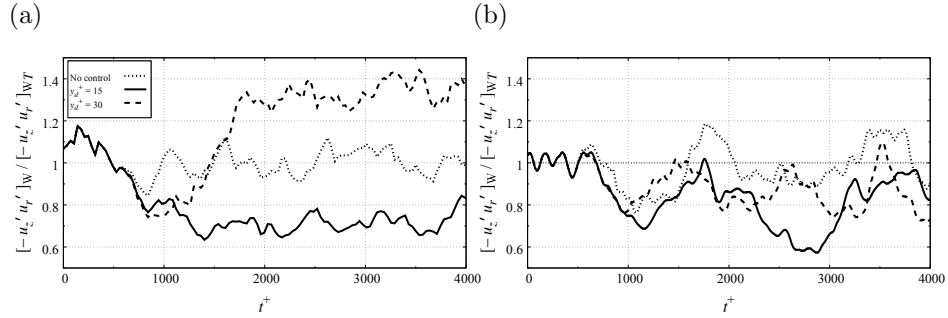


Figure 14: Time trace of the integral value of the weighted Reynolds shear stress: (a) $\gamma = 5$, (b) $\gamma = 17$.

Figure 14 shows the time trace of the integral value of the weighted RSS. Here, integral operator of $[\]_W$ is defined by

$$[\phi]_W = \frac{1}{f(a)} \int_a^{a+1} (a+1-r)\langle\phi\rangle r dr, \quad (23)$$

$[\phi]_{WT}$ is the temporal average of the uncontrolled $[\phi]_W$. The control with time relaxation is applied from $t^+ = 500$. Focusing on the case of $\gamma = 5$, $[-u'_z u'_r]_W$ (normalized by $[-u'_z u'_r]_{WT}$) at $y_d^+ = 15$ decreases monotonically after the start of control and eventually converges to about 0.7. In addition, $[-u'_z u'_r]_W$ at $y_d^+ = 30$ decreases similarly to the case of $y_d^+ = 15$ immediately after the start of control, rapidly increases from $t^+ = 1200$, and finally converges to about 1.3. Chung *et al.* [3] reported that even with a high detection plane where drag increases, reducing the strength of blowing and suction can achieve the drag reduction effect. $[-u'_z u'_r]_W$ at $y_d^+ = 30$ decreases once immediately after the control ($500 \leq t^+ \leq 1000$) because the strength of blowing and suction is minimal. In the case of $\gamma = 17$, $[-u'_z u'_r]_W$ at $y_d^+ = 15$ and 30 decreases to the range of 0.8 to 0.9. In all of the cases, the increase or decrease in $[-u'_z u'_r]_W$ corresponds to the change in skin-friction drag.

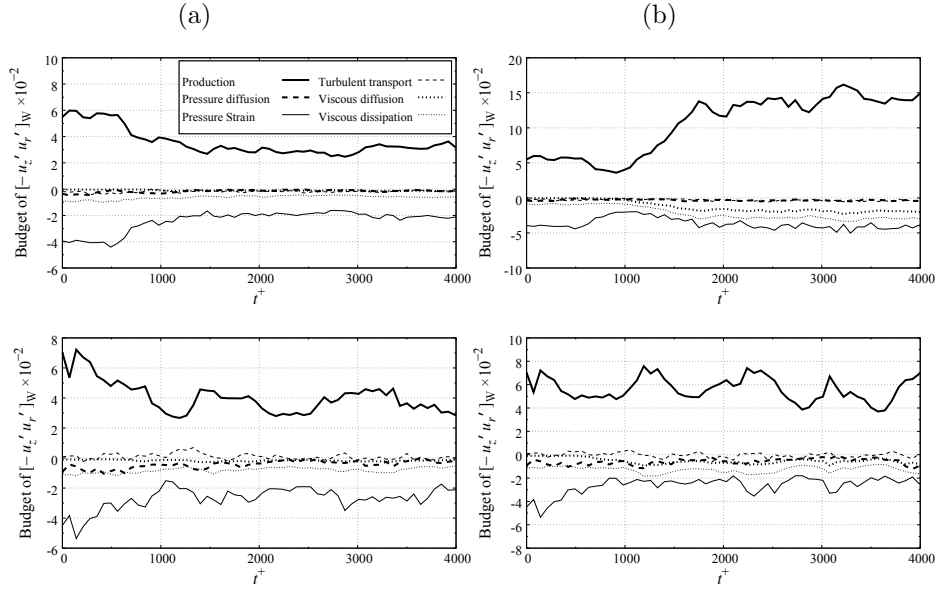


Figure 15: Time trace of transport of the weighted Reynolds shear stress at (top row) $\gamma = 5$ and (bottom row) $\gamma = 17$: (a) $y_d^+ = 15$, (b) $y_d^+ = 30$.

An analysis of transport of the weighted RSS is conducted to identify the factors that caused the RSS to change over time. The transport equation of the RSS is written as:

$$\begin{aligned}
\frac{\partial \langle -u'_z u'_r \rangle}{\partial t} &= \underbrace{\langle u'_r u'_r \rangle \frac{\partial \langle u_z \rangle}{\partial r}}_{\text{Production}} + \underbrace{\left\langle -p' \left(\frac{\partial u'_r}{\partial z} + \frac{\partial u'_z}{\partial r} \right) \right\rangle}_{\text{Pressure strain}} + \underbrace{\frac{\partial \langle u'_r p' \rangle}{\partial z} + \frac{\partial \langle u'_z p' \rangle}{\partial r}}_{\text{Pressure diffusion}} \\
&+ \underbrace{\frac{1}{r} \frac{\partial}{\partial r} (r \langle u'_r u'_z u'_r \rangle) - \frac{\langle u'_z u'_\theta u'_\theta \rangle}{r}}_{\text{Turbulent transport}} \\
&+ \underbrace{\frac{1}{\text{Re}_b} \left\{ \frac{1}{r} \frac{\partial}{\partial r} \left(r \frac{\partial \langle -u'_z u'_r \rangle}{\partial r} \right) + \frac{\langle u'_z u'_r \rangle}{r^2} \right\}}_{\text{Viscous diffusion}} \\
&+ \underbrace{\frac{2}{\text{Re}_b} \left\langle \frac{\partial u'_r}{\partial r} \frac{\partial u'_z}{\partial r} + \frac{1}{r} \frac{\partial u'_z}{\partial \theta} \left(\frac{1}{r} \frac{\partial u'_r}{\partial \theta} - \frac{u'_\theta}{r} \right) + \frac{\partial u'_r}{\partial z} \frac{\partial u'_z}{\partial z} \right\rangle}_{\text{Viscous dissipation}}. \quad (24)
\end{aligned}$$

By applying $[\]_W$ to both sides of Eq. (24), the transport equation relating to the turbulent contribution of the skin-friction coefficient is obtained. Figure 15

shows time trace of each term applied by $[\]_w$. The vertical axis is nondimensionalized by twice of the bulk velocity and the boundary layer thickness. In
310 the case of $\gamma = 5$, the production term decreases at $y_d^+ = 15$ and increases at
 $y_d^+ = 30$, indicating that there is correlation between the changes in production
term and the weighted RSS. In addition, following the change of the production
term, the pressure strain changes at $y_d^+ = 15$, and the viscous diffusion and vis-
cous dissipation change at $y_d^+ = 30$. Although the production term at $y_d^+ = 30$
315 hardly changes qualitatively, it is slightly reduced as compared to that in the
uncontrolled case when evaluated by the temporal average. From these results,
it is clarified that the factor of the temporal change of the weighted RSS is the
production term.

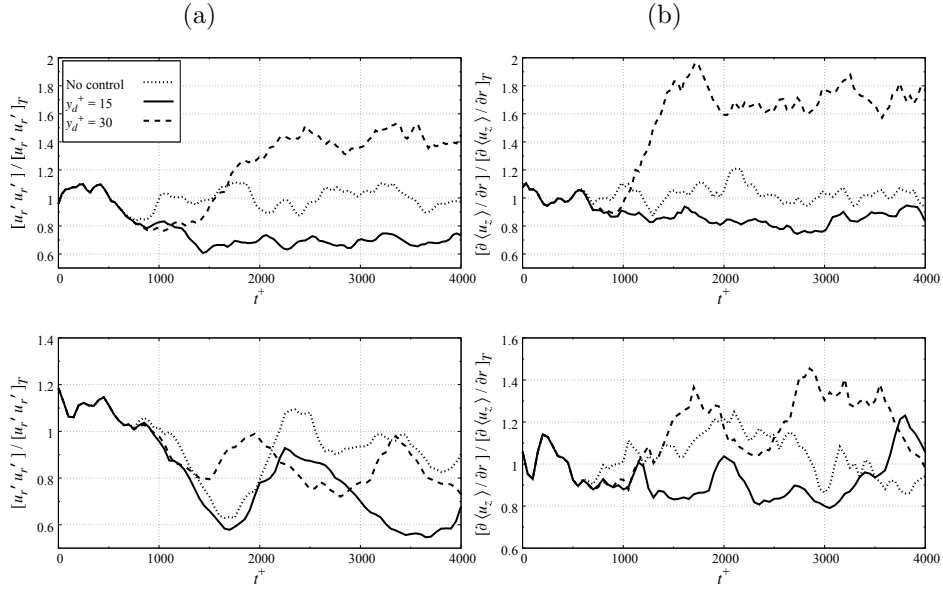


Figure 16: Time trace of contribution to the RSS production at (top row) $\gamma = 5$ and (bottom row) $\gamma = 17$: (a) radial turbulent kinetic energy, (b) mean velocity gradient.

The production term of the RSS is composed of the product of radial turbulent kinetic energy ($\text{TKE}_r, \langle u_r' u_r' \rangle$) and average velocity gradient (MVG, $\partial \langle u_z \rangle / \partial r$). Figure 16 shows the time trace of the TKE_r and MVG spatially averaged in the radial direction. In the results of $\gamma = 5$, at $y_d^+ = 15$, TKE_r and MVG decrease to about 0.7 and 0.8, respectively, and at $y_d^+ = 30$, these increase to about 1.4 and 1.8. Therefore, at $y_d^+ = 15$, the TKE_r greatly contributes to the reduction of the production term, while at $y_d^+ = 30$, the increment of the MVG contributes to the increase in the production term. Focusing on the case of $\gamma = 17$, the TKE_r and MVG decrease at $y_d^+ = 15$, while the MVG slightly increases at $y_d^+ = 30$. Since the drag reduction rate at $y_d^+ = 30$ is about 10%, the TKE_r is more related to the change in the production term than the MVG. These results for two different curvatures reveal that when the drag decreases, TKE_r greatly contributes to the reduction in the production term, and similarly when the drag increases, the MVG contributes to the increase.

The reason that the production term is reduced by the opposition control is

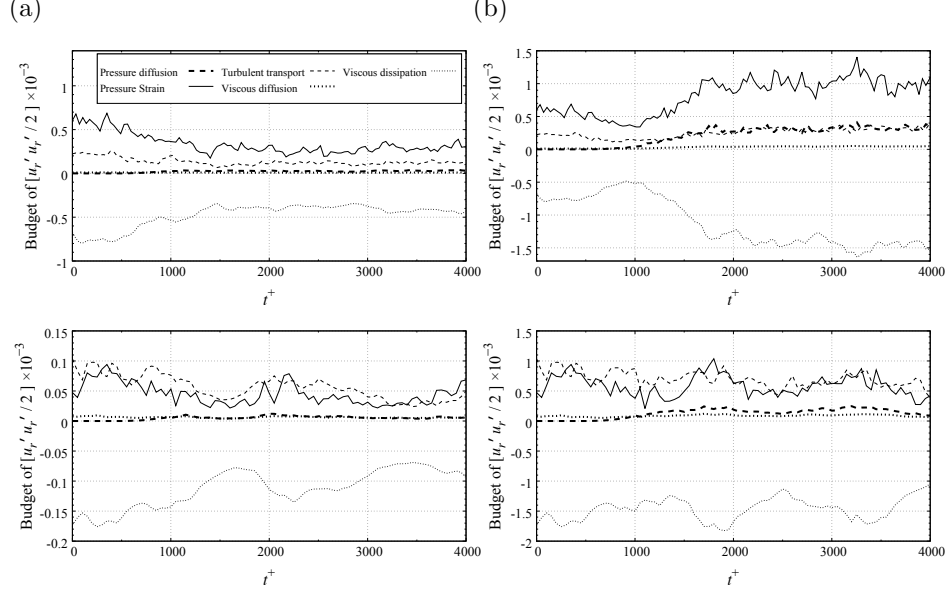


Figure 17: Time trace of transport of the radial turbulent kinetic energy at (top row) $\gamma = 5$ and (bottom row) $\gamma = 17$: (a) $y_d^+ = 15$, (b) $y_d^+ = 30$.

that TKE_r is attenuated. The transport equation of TKE_r is given by

$$\begin{aligned}
 \frac{\partial}{\partial t} \left(\frac{1}{2} \langle u_r' u_r' \rangle \right) &= \underbrace{\left\langle \frac{p'}{r} \frac{\partial}{\partial r} (r u_r') \right\rangle}_{\text{Pressure strain}} + \underbrace{\left\langle -\frac{1}{r} \frac{\partial}{\partial r} (r \langle u_r' p' \rangle) \right\rangle}_{\text{Pressure diffusion}} \\
 &+ \underbrace{\frac{1}{2} \left\langle -\frac{1}{r} \frac{\partial}{\partial r} (r \langle u_r' u_r' u_r' \rangle) + \frac{2}{r} \langle u_r' u_\theta' u_\theta' \rangle \right\rangle}_{\text{Turbulent transport}} \\
 &+ \underbrace{\frac{1}{2\text{Re}_b} \left\langle \frac{1}{r} \frac{\partial}{\partial r} \left(r \frac{\partial \langle u_r' u_r' \rangle}{\partial r} \right) + \frac{2 \langle u_\theta' u_\theta' - u_r' u_r' \rangle}{r^2} \right\rangle}_{\text{Viscous diffusion}} \\
 &+ \underbrace{\frac{-1}{\text{Re}_b} \left\langle \left(\frac{\partial u_r'}{\partial r} \right)^2 + \left(\frac{u_\theta'}{r} - \frac{1}{r} \frac{\partial u_r'}{\partial \theta} \right)^2 + \left(\frac{\partial u_r'}{\partial z} \right)^2 \right\rangle}_{\text{Viscous dissipation}}. \quad (25)
 \end{aligned}$$

Figure 17 is representing time trace of each term applied by []. Initially, considering the case of $\gamma = 5$, the pressure strain at $y_d^+ = 15$ is greatly attenuated, the
335 turbulent transport decreases and viscous dissipation increases. At $y_d^+ = 30$, the trend is opposite to the change at $y_d^+ = 15$, while the pressure diffusion

changes significantly due to the increased strength of blowing and suction. Subsequently, in the case of $\gamma = 17$, no qualitative change is observed. However, the pressure strain decreased by about 30% at $y_d^+ = 15$ and about 5% at $y_d^+ = 30$.
³⁴⁰ In particular, for $y_d^+ = 30$, the drag reduction rate of about 10% is obtained despite the slight reduction in the pressure strain. Thus, these results clarify that the reduction of the pressure strain contributes to the decline of drag even in the case of large curvature. Therefore, the drag reduction mechanism is not affected by the curvature.

345 4. Conclusion

The DNS of opposition-controlled turbulent flow along the controlled cylinder was performed to investigate the effect of wall curvature on the control effect. Many studies have reported that $y_d^+ = 15$ is the optimal height of the detection plane for the channel flow, and similar results were obtained in cases
350 where the curvature is large. However, the drag reduction rate decreases as the curvature increases. Further, when the curvature is large, the turbulence intensity is lower than that of the channel flow, and therefore a high drag reduction rate is obtained even on the detection plane far from the wall.

In opposition control for turbulent flow along the cylinder, the peak values of the radial turbulence intensity and radial vorticity intensity are linearly
355 related to the drag reduction rate. However, the peak values of radial turbulence intensity are not distributed on the same linear line but are organized by the curvature. Accordingly, the turbulence intensity decreases as the curvature increases. On the other hand, the peak value of the vorticity intensity was
360 distributed on the same straight line.

The FIK identity as well as transport of weighted RSS and turbulent kinetic energy reveal that the drag reduction mechanism is similar to that of channel flow. Due to the opposition control, the turbulent contribution of C_f^T changes significantly, while the other contributions of C_f^D and C_f^W barely change. In
365 addition, it is found that even when the curvature is large, the cause of drag reduction is the decrease in radial pressure strain. The decrease in radial pressure strain causes decrease in the radial turbulent kinetic energy, RSS production term, and RSS, which in turn contribute to reduction in the drag coefficient.

Acknowledgments

370 This research was partially supported by the Ministry of Education, Culture, Sports, Science, and Technology through a Grant-in-Aid for Scientific Research (A) of JP18H03758 in 2019.

- [1] H. Choi, P. Moin, J. Kim, Active turbulence control for drag reduction in wall-bounded flows, *Journal of Fluid Mechanics* 262 (1994) 75–110.
- 375 [2] E. P. Hammond, T. R. Bewley, P. Moin, Observed mechanisms for turbulence attenuation and enhancement in opposition-controlled wall-bounded flows, *Physics of Fluids* 10 (1998) 2421–2423.
- [3] Y. M. Chung, T. Talha, Effectiveness of active flow control for turbulent skin friction drag reduction, *Physics of Fluids* 23 (2011) 025102.
- 380 [4] B. Q. Deng, C. Xu, W. X. Huang, G. Cui, Strengthened opposition control for skin-friction reduction in wall-bounded turbulent flows, *Journal of Turbulence* 15 (2014) 122–143.
- [5] M. Ge, D. Tian, L. Yongqian, Dynamic evolution process of turbulent channel flow after opposition control, *Fluid Dynamics Research* 49 (2016) 015505.
- 385 [6] Y. S. Wang, W. X. Huang, C. X. Xu, Active control for drag reduction in turbulent channel flow: the opposition control schemes revisited, *Fluid Dynamics Research* 48 (2016) 055501.
- [7] A. Stroh, B. Frohnepfel, P. Schlatter, Y. Hasegawa, A comparison of opposition control in turbulent boundary layer and turbulent channel flow, *Physics of Fluids* 27 (2015) 075101.
- 390 [8] Q. J. Xia, W. X. Huang, C. Xu, G. Cui, Direct numerical simulation of spatially developing turbulent boundary layers with opposition control, *Fluid Dynamics Research* 47 (2015).
- [9] J. C. Neves, P. Moin, R. D. Moser, Effects of convex transverse curvature on wall-bounded turbulence. part 1. the velocity and vorticity, *Journal of Fluid Mechanics* 272 (1994) 349–382.
- 395 [10] J. C. Neves, P. Moin, Effects of convex transverse curvature on wall-bounded turbulence. part 2. the pressure fluctuations, *Journal of Fluid Mechanics* 272 (1994) 383–406.
- 400

- [11] J. Piquet, V. C. Patel, Transverse curvature effects in turbulent boundary layer, *Progress in Aerospace Sciences* 35 (1999) 661–672.
- [12] N. Afzal, R. Narasimha, Asymptotic analysis of thick axisymmetric turbulent boundary layers, *AIAA Journal* 23 (1985) 963–965.
- 405 [13] S. Monte, P. Sagaut, T. Gomez, Analysis of turbulent skin friction generated in flow along a cylinder, *Physics of Fluids* 23 (2011) 065106.
- [14] K. Fukagata, K. Iwamoto, N. Kasagi, Contribution of Reynolds stress distribution to the skin friction in wall-bounded flows, *Physics of Fluids* 14 (2002) 73–76.
- 410 [15] T. Ohta, Turbulence structures in high-speed air flow along a thin cylinder, *Journal of Turbulence* 18 (2017) 497–511.
- [16] K. Fukagata, N. Kasagi, Highly energy-conservative finite difference method for the cylindrical coordinate system, *Journal of Computational Physics* 181 (2002) 478–498.
- 415 [17] F. E. Ham, F. S. Lien, A. B. Strong, A fully conservative second-order finite difference scheme for incompressible flow on nonuniform grids, *Journal of Computational Physics* 177 (2002) 117–133.
- [18] P. R. Spalart, R. D. Moser, M. M. Rogers, Spectral methods for the navier-stokes equations with one infinite and two periodic directions, *Journal of Computational Physics* 96 (1991) 297–324.
- 420 [19] K. Fukagata, N. Kasagi, P. Koumoutsakos, A theoretical prediction of friction drag reduction in turbulent flow by superhydrophobic surfaces, *Physics of Fluids* 18 (2006) 051703.
- [20] J. Kim, P. Moin, R. Moser, Turbulence statistics in fully developed channel flow at low Reynolds number, *Journal of Fluid Mechanics* 177 (1987) 133–166.
- 425

Nomenclature

	[]	Volume average
	[] _w	Integral operator
430	δ	Boundary layer thickness
	δ^*	Displacement thickness
	γ	Curvature defined by ratio of δ to a
	$\langle -u'v' \rangle$	Reynolds shear stress of channel flow
	$\langle -u'_z u'_r \rangle$	Reynolds shear stress of flow along a cylinder
435	$\langle \rangle$	Uniform-spatial average
	\mathcal{T}	Relaxation time in opposition control
	ν	Kinematic viscosity
	ϕ	Arbitrary
	p'	Pressure fluctuation
440	Re_a	Reynolds number based on u_∞ and a
	Re_b	Reynolds number based on u_b and 2δ
	Re_δ	Reynolds number based on u_∞ and δ
	Re_τ	Reynolds number based on u_τ and δ
	ρ	Density
445	τ_w	Wall shear stress
	θ	Azimuthal coordinate
	ε	Viscous dissipation
	+	Normalization of wall coordinates

	*	Dimensional variable
450	A	Strength of wall blowing and suction
	a	Cylinder radius
	$C_{f,b}$	Skin-friction coefficient based on u_b
	$C_{f,\infty}$	Skin-friction drag coefficient based on u_∞
	d	Diffusion term
455	$f(a)$	Shape factor
	G	Energy gain
	h	Convection term
	L_z	Computational domain in axial direction
	N_θ	Number of computational grid points in azimuthal direction
460	N_r	Number of computational grid points in radial direction
	N_z	Number of computational grid points in axial direction
	P	Mean pressure
	p	Pressure
	Q	Second invariant of the velocity gradient tensor
465	r	Radial coordinate
	$R(u'_z, u'_z)$	Azimuthal two-point correlation of the axial velocity
	R_D	Drag reduction rate
	S	Net energy saving rate
	t	Time
470	u_∞	Free-stream velocity

	u_τ	Wall-friction velocity
	u_θ	Azimuthal velocity
	u_b	Bulk velocity
	u_r	Radial velocity
475	u_z	Axial velocity
	$u_{r,w}$	Wall-normal velocity on the wall
	v	Wall-normal velocity of channel flow
	y	Wall-normal coordinate
	y_d	Detection plane height in opposition control
480	z	Axial coordinate